Fuel 408 (2026) 137768

Contents lists available at ScienceDirect

Fuel

journal homepage: www.elsevier.com/locate/fuel

Full Length Article

Dual-Regulated Ru by alloying and Metal-Substrate interaction for Energy-Efficient hydrazine Oxidation-Paired hydrogen production

Qijing Zhang [a], Hongxia Yu [a], Siyi Wang [a], Haibo Li [a], Suyuan Zeng [a], Rui Li [a], Qingxia Yao [a], Qi Zhang [a], Ruru Chen [a,*], Lijian Meng [b,*], Konggang Qu [a,*]

[a] School of Chemistry and Chemical Engineering, Shandong Provincial Key Laboratory/Collaborative Innovation Center of Chemical Energy Storage & Novel Cell Technology, Liaocheng University, Liaocheng 252059, China
[b] Centre of Innovation in Engineering and Industrial Technology, Instituto Superior de Engenharia do Porto, Instituto Politecnico do Porto 4249-015 Porto, Portugal

ARTICLE INFO

Keywords:
RuPd alloy
Hydrogen evolution
Hydrazine oxidation
Metal-Substrate Interaction
Dual Engineering

ABSTRACT

Overall water splitting (OWS) is the most potential method for large-scale hydrogen production, but the high-potential and sluggish oxygen evolution reaction (OER) greatly impedes its efficacy. Coupling the low-potential hydrazine oxidation reaction (HzOR) with the cathodic hydrogen evolution reaction (HER) has drawn widespread attention with energy-saving advantage and safe products, which necessitates the elaborate design of advanced bifunctional electrocatalysts. Herein, only using two complexes of Ru and Pd with 2,2′-bipyridine, the novel RuPd alloy/N-codoped carbon (RuPd/NC) composite was originally synthesize by direct mixing and pyrolysis, showing superior dual activity for HER and HzOR. Particularly, to deliver the current density of 10 mA cm^{-2}, RuPd/NC merely needs the potentials of −8 and −42 mV for alkaline HER and HzOR, far outperforming Pt/C and being most advanced among the previously studied counterparts. Moreover, the two-electrode overall hydrazine splitting (OHzS) needs ultrasmall voltages of 0.042 and 0.239 V to achieve 10 and 100 mA cm^{-2}, displaying great energy-saving feature. Moreover, the better activity for neutral HER, HzOR and OHzS on RuPd/NC was also found compared with Pt/C. The theoretical simulations uncover the water dissociation at Ru site with the greatly reduced energy barrier followed by the H desorption on the adjacent Pd site for HER, and the optimum activation energy on Ru site for HzOR, crediting to the synergistic regulation of alloying effect and metal-substrate interaction.

1. Introduction

To date, the excessive consumption of fossil fuels has aggravated energy crisis and global warming. Hydrogen is now deemed as the perfect alternative on account of the highest energy density and carbon-free characteristics [1,2]. However, although high-purity hydrogen can be obtained by conventional overall water splitting (OWS), the anodic oxygen evolution reaction (OER) with sluggish 4-electron transfer and high potential greatly hinders the efficiency of OWS [3,4]. Recently, developing small-molecule oxidation reactions to replace OER has been regarded as one effective solving approach [5], including urea [6,7], alcohols [8,9], biomass[10,11] and hydrazine [12]. Particularly, hydrazine oxidation reaction (HzOR) exhibits a significantly low thermodynamic potential (−0.33 V vs. RHE) [13], which can facilitate highly efficient H_2 production by integrating cathodic hydrogen evolution reaction (HER) to assemble the novel overall hydrazine splitting (OHzS) cell [14,15]. More importantly, the non-toxic and safe N_2 generated in HzOS would avert the explosion risk of electrolyzer and also simplify the device [16]. From this point of view, it is of great significance to develop highly active and stable materials for bifunctional HER and HzOR together with instructive structure–activity relationships.

Noble-metal Pt has widely served as the advanced electrocatalysts for HER and HzOR [17], its fancy price and scarcity yet remain one of most significant challenge of related techniques. Ru is one of the Pt-group metals with Pt-like catalytic activity, but only costs a third of the price of Pt [18,19], and the exploration of Ru-based materials would be greatly potential for the high-performance electrocatalyst for HER and HzOR with favored cost performance [20,21]. The mono-metallic active site is often insufficient in the development of bifunctional catalysts, owing to the multiple intermediate reactions involved in HER and HzOR. In this case, alloying can provide multiple reaction sites, and more particularly, can effectively regulate the electronic property of

* Corresponding authors.
E-mail addresses: chenruru@lcu.edu.cn (R. Chen), ljm@isep.ipp.pt (L. Meng), qukonggang@lcu.edu.cn (K. Qu).

https://doi.org/10.1016/j.fuel.2025.137768
Received 29 September 2025; Received in revised form 19 November 2025; Accepted 26 November 2025
Available online 29 November 2025

metals [22–24]. Additionally, to maximize atomic utilization is a key method to boost the cost-effectiveness of catalysts, which can be achieved by loading metal phases on the reasonable carbon substrate [25,26], which can thus facilitate the dispersion of the metal phase, improve stability, and also regulate its electronic properties by the strong metal-substrate interaction [27,28]. Therefore, to rationally design the simple strategy for the Ru alloy loaded in carbon substrate is imperative for the advanced bifunctional electrocatalysts.

Herein, the complexes of Ru and Pd with 2,2′-bipyridine were selected as the precursors to synthesize RuPd alloy/N-codoped carbon (RuPd/NC) by facile mixing and pyrolysis. The easily prepared RuPd/NC features alloy particles of 4.5 nm, large surface area and highly graphitized doped carbon. Benefiting from the synergistic regulation of alloying effect and metal-substrate interaction, RuPd/NC displays outstanding bifunctional HER and HzOR activity in nonacidic electrolytes. Concretely, to achieve 10 mA cm^{-2}, RuPd/NC just has the potentials of 27 and −42 mV for alkaline HER and HzOR, both far superior to Pt/C, together with the matchable neutral HER activity and better HzOR activity compared to Pt/C. Moreover, the two-electrode OHzS system separately need small voltages of 0.042 and 0.267 V in alkaline and neutral electrolytes, largely superior to Pt/C with huge energy-saving advantages relative to the OWS system, facilely operated under a home-made hydrazine H_2O_2 fuel cell (DHHPFC) to produce H_2 of 1.139 mmol h^{-1}. The theoretical computations elucidate the water dissociation of HER occurs with the much-reduced energy barrier at Ru site followed by the H desorption on the adjacent Pd site, while HzOR occurs on Ru site of RuPd/NC with the lowest activation energy.

2. Experimental section

2.1. Chemicals and materials

Tris (2,2-bipyridine) ruthenium (II) chloride ($Ru(bpy)_3Cl_2$) and (2,2′-bipyridine)dichloropalladium(II) ($Pd(bpy)Cl_2$) were purchased from Shanghai Aladdin Industrial Corporation. The commercial 20 % Pt/C, Nafion solution and Nafion 115 membrane were obtained from Gaoss Union (TianJin) Photoelectric technology CO., LTD.

2.2. Preparation of RuPd/NC

Typically, 27.2 mg $Pd(bpy)Cl_2$ and 272.7 mg $Ru(bpy)_3Cl_2$ were dispersed in 20 mL ethanol and 15 mL Milli-Q water and stirred for 24 h followed with rotary drying, and then treated with pyrolysis at 900 °C for 3h under Ar atmosphere to obtain RuPd/NC.

2.3. Preparation of Ru/N-doped carbon (Ru/NC) and Pd/N-doped carbon (Pd/NC)

3 mg $Ru(bpy)_3Cl_2$ was directly treated with pyrolysis at 900 °C for 3 h in Ar atmosphere, the collected sample were named as Ru/NC. Pd/NC was synthesized using the similar process with 70 mg $Pd(bpy)Cl_2$ as the precursor.

2.4. Physical characterizations

A Talos F200X G2 microscope (TEM) was employed for transmission electron microscope (TEM), high-resolution TEM (HRTEM) and elemental mapping analyses. A SmartLab (9 kW) diffractometer was used for powder X-ray diffraction (XRD) and a HORIBA iHR550 spectrometer with an excitation wavelength of 532 nm for Raman analysis. Surface chemistry was examined with a Kratos Axis Ultra X-ray photoelectron spectrometer (XPS). The specific surface areas were derived from N_2 adsorption–desorption isotherms recorded on a Micromeritics 2460 analyzer based on the Brunauer-Emmett-Teller (BET) method.

X-ray absorption (XAS) measurements were carried out at the Shanghai Synchrotron Radiation Facility. Raw spectra were processed and the extended X-ray absorption fine structure (EXAFS) region modelled with the ATHENA and ARTEMIS modules of the Demeter software suite. Energy alignment was verified against Ru and Pd reference foils. The energy calibration of the sample was conducted through standard Ru foil and Pd foil, which as a reference was simultaneously measured. After background removal and edge-step normalization, k^3-weighted signals were Fourier-transformed (Hanning window, dk = 1.0 Å) over 3–14.1 $Å^{-1}$ for Ru and 3–10.0 $Å^{-1}$ for Pd. The amplitude-reduction factor S_0^2 was fixed to the values extracted from fits of the corresponding metal foils (0.878 for Ru, 0.874 for Pd) to extract the coordination number (CN).

2.5. Electrochemical measurements

The electrochemical measurements were performed using an electrochemical station (References 3000, Gamry Instruments, USA) coupled to a rotating disk electrode (RDE) apparatus under ambient conditions. The working electrode was fabricated by casting 20 μL of a well-dispered catalyst ink (2 mg mL^{-1}) onto a mirror-polished RDE and drying naturally, followed with the addition of 0.5 wt% Nafion solution (5 μl). The reference was an Ag/AgCl (3.5 M KCl) electrode, and a graphite rod served as the counter electrode. 1 M KOH solution was employed for the HER electrolyte and 1 M KOH + 0.5 M N_2H_4 for the HzOR electrolyte. Except for stability experiments, all recorded data were iR-compensated.

In the DHHPFC configuration, catalyst inks were deposited on Sigracet 29BC carbon paper (1 cm × 2 cm) at 1 mg cm^{-2}; the anode employed either RuPd/NC or commercial Pt/C, while the cathode consistently used Pt/C. During operation, a 0.5 M H_2SO_4 + 5 M H_2O_2 catholyte and a 4 M KOH + 1 M N_2H_4 anolyte were fed at 5 mL min^{-1} into their respective chambers, separated by a Nafion N115 membrane, via a dual-channel peristaltic pump (EC200-01, Gaoss Union).

The solar cell-powered OHzS setup is built from three components: a two-electrode OHzS module that uses RuPd/NC catalysts at both electrodes and an electrolyte of 1 M KOH + 0.5 M N_2H_4; a commercial polycrystalline-silicon photovoltaic panel rated at 1.5 V; and a 150 W xenon lamp light source (CEL-PF300-T9, Beijing China Education Au-Light Co., Ltd.). The lamp delivers 2 Sun irradiances (2 × 1000 W m^{-2}) over the 300–2500 nm range onto the solar cell.

2.6. Calculation methods of ECSA-normalized activity and mass activity

$ECSA = C_{dl} / C_s$.

where C_{dl} is general specific capacitance, C_s value was generally found to be in the range of 20−60 μF cm^{-2} and the capacitance of 40 μF cm^{-2} was used to calculate the ECSA.

$Mass\ activity = j / mass_{metal}$.

The calculations of mass activity (A mg^{-1}) were performed based on the catalyst loading density $mass_{Ru}$ and the current density j (mA cm^{-2}) at varied overpotential.

2.7. Theoretical calculations

All computations relied on density functional theory (DFT) as implemented in the Quantum-Espresso code. Structural relaxation was per_x0002_formed by using spin-polarized scalar relativistic ultrasoft pseudopotentials and an exchange correlation functional in the form of a Perdew-Burke Ernzerhof functional with the van der Waals interaction by the empirical dispersion correction. Vacuum regions of at least 20 and 15 Å in vertical and parallel directions, respectively, were applied to avoid unphysical in_x0002_teractions between periodic images. All calculations were conducted with a plane wave cutoff of 60 rydberg and a 5 × 5 × 1 Monkhorst-Pack k-grid for the Brillouin zone[2], which are sufficient to ensure convergence. Geometry optimization was performed using a quasi-Newton algorithm. A total energy convergence of 1.4 × 10^{-4} eV and residual forces below 0.02 eV $Å^{-1}$ were achieved. More

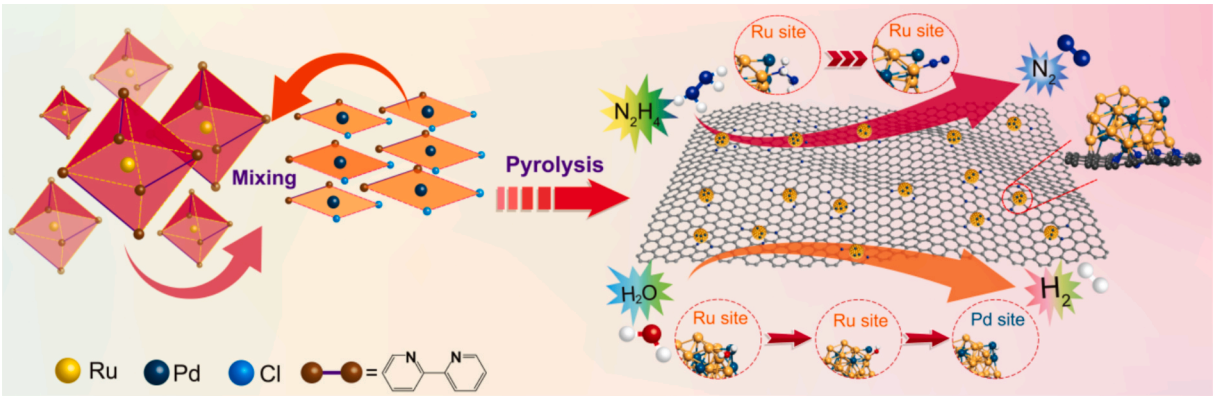

Scheme. 1. Schematic preparation route of RuPd/NC for bifunctional HER and HzOR.

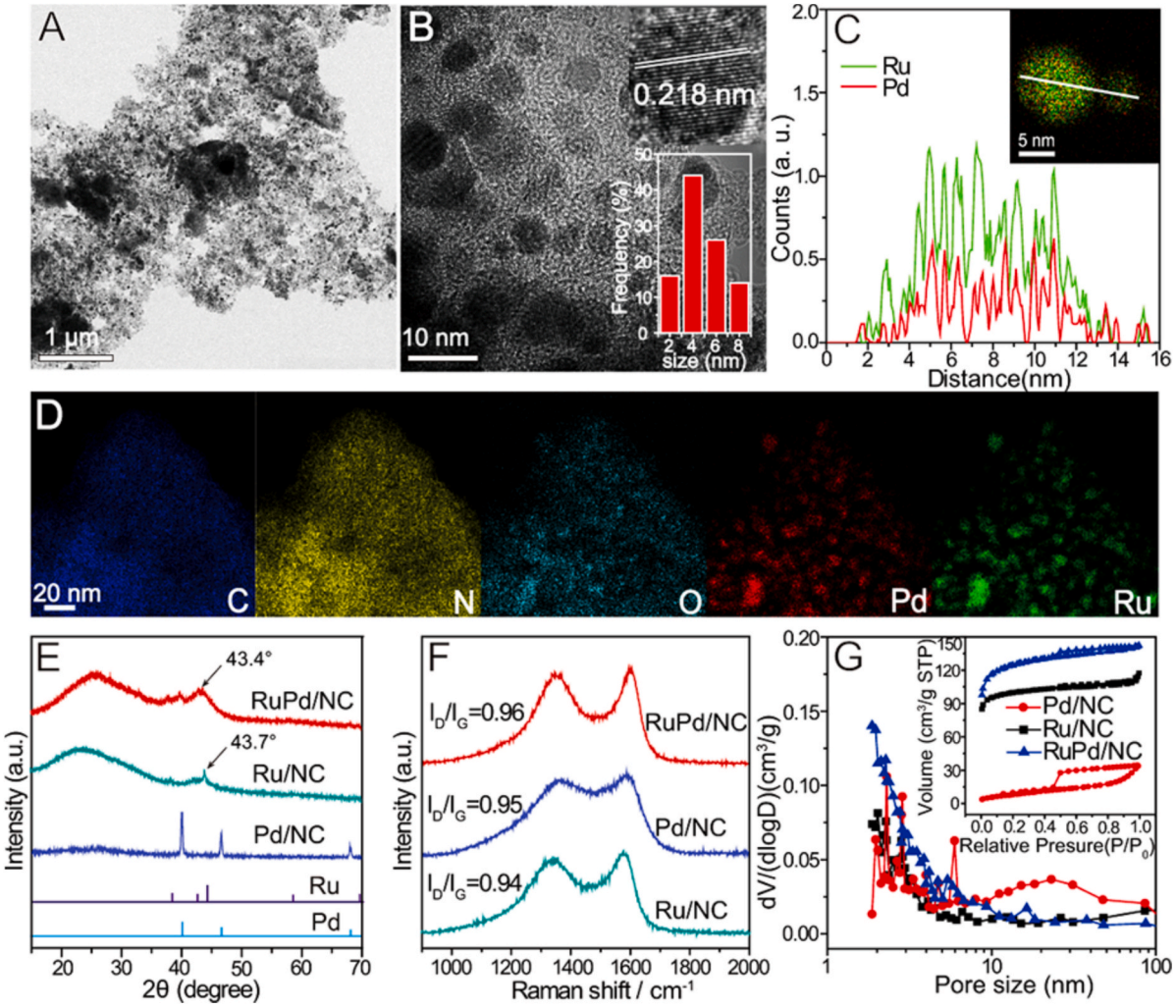

Fig. 1. (A-B) TEM images in different magnifications, with the inset showing the size distribution of nanoparticles and (C) the line-scan elemental distribution curves for RuPd/NC. (D) TEM elemental mapping images of C, N, O, Pd and Ru for RuPd/NC. (E) XRD patterns, (F) Raman spectra and (G) the N_2 adsorption–desorption isotherms and the pore size distribution curves of different samples.

computational details were presented in the supporting information.

3. Results and discussion

Scheme 1 illustrated that the RuPd/NC was obtained through a direct "mix-and-pyrolyze" strategy. The morphological information of RuPd/NC was initially analyzed through TEM. Fig. 1A presents two-dimensional carbon flakes dotted with dense nanoparticles for RuPd/NC composite. The HRTEM image (Fig. 1B) displays fine particles with the even size of 4.4 nm and high-degree crystalline phase with a spacing of 0.218 nm, not associated with sole Pd or Ru metal but well matchable with that of RuPd alloy (0.219 nm) [29,30]. The line-scan elemental

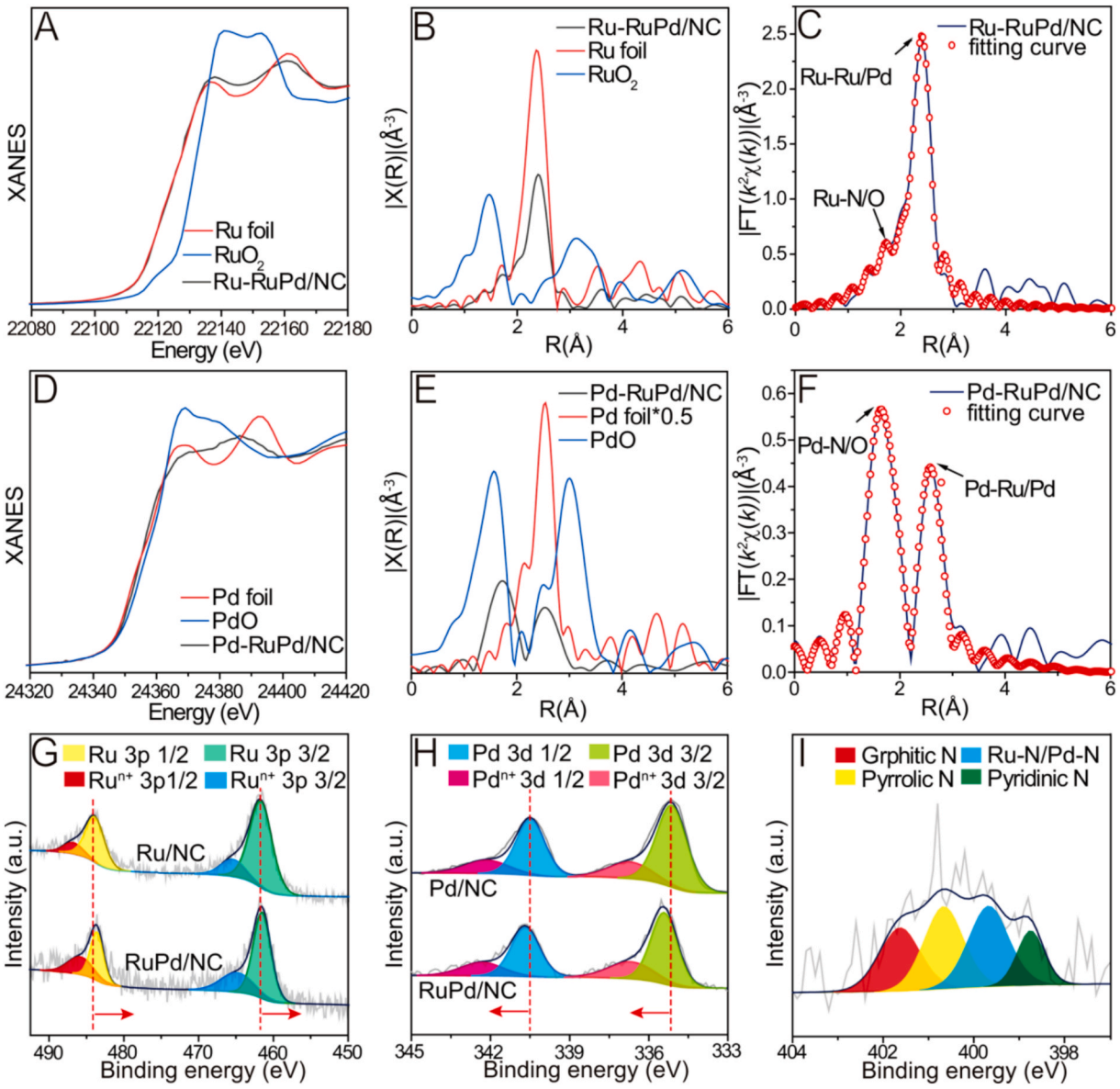

Fig. 2. (A) Ru K-edge XANES and (B) Fourier transform (FT) of the Ru K-edge EXAFS spectra of RuPd/NC, Ru foil and RuO_2. (C) The EXAFS fitting results of RuPd/NC at R space. (D) Pd K-edge XANES and (E) Fourier transform (FT) of the Pd K-edge EXAFS spectra of RuPd/NC, Ru foil and RuO_2. (F) The EXAFS fitting results of RuPd/NC at R space. (G) Ru 3p of RuPd/NC and Ru/NC, (H) Pd 3d of RuPd/NC and Pd/NC and (I) XPS N 1 s spectra of RuPd/NC.

distribution curves clearly confirm the uniform dispersion of Ru and Pd elements with the intensity ratio of Ru and Pd of about 2:1 (Fig. 1C). The TEM elemental mapping images (Fig. 1D) reveal the even-distributed C, N, O, Pd and Ru elements, while the perfect overlap of Ru and Pd components firmly proves the formation of RuPd alloy. Comparatively, the small Ru nanoparticles of 1.8 nm can be found on Ru/NC (Fig. S1), while Pd/NC owns the large aggregates of Pd particles (Fig. S2).

The metallic components were then examined by XRD. Fig. 1E presents the diffraction peaks at 40.1, 46.7 and 68.1° for Pd/NC separately coincide with (111), (200) and (220) planes of Pd (JCPDS No. 46–1043) [31], and the diffraction peaks at 38.4, 42.2 and 44.0° for Ru/NC correlate with (100) (002) and (101) planes of Ru (JCPDS No. 06–0663) [26], respectively. In comparison, the signal positions of RuPd/NC slightly shift to the left relative to Ru/C, arising from the successful introduction of larger Pd atoms into the Ru lattice [32]. The carbon skeleton structure was further examined with Raman spectra. As illustrated in Fig. 1F, the intensity ratio of D band to G band (I_D/I_G) values are in the range of 0.94−0.96, indicating the highly graphitized carbons for all samples [33]. The surface properties were probed by N_2 adsorption–desorption isotherms (Fig. 1G and Table S1). All samples show the characteristics of type-IV adsorption–desorption curve with the typical hysteresis loop, suggesting the abundant porosity. Distinctly, RuPd/NC owns the largest BET surface area of 380.98 $m^2\ g^{-1}$ with the pore volume of 0.05 $cm^3\ g^{-1}$, relative to Ru/NC (305.27 $m^2\ g^{-1}$ and 0.03 $cm^3\ g^{-1}$) and Pd/NC (31.62 $m^2\ g^{-1}$ and 0.05 $cm^3\ g^{-1}$).

XAS was further conducted to understand the coordination environment of metals in RuPd/NC. Fig. 2A depicts the X-ray absorption near-edge structure (XANES) of Ru in RuPd/NC with the K-edge location near to Ru foil, and Ru mainly exists with an average valence state of 0 in RuPd/NC. Figs. 2B and 2C show the Fourier-transformed EXAFS spectra of Ru in RuPd/NC. A distinct signal at 2.66 Å is associate with the Ru-Ru/Pd bond by a CN of 6.6 (Table S2), much less than that of bulk Ru (CN=12), while the signal at 2.00 Å coincide with the Ru-N/O bond by the CN of 2.1 [27,34]. Similarly, the K-edge position of Pd in the RuPd/NC is between the Pd foil and PdO (Fig. 2D). The EXAFS spectra of Pd in RuPd/NC display the Pd-Ru/Pd bond locating at 2.79 Å with the CN of

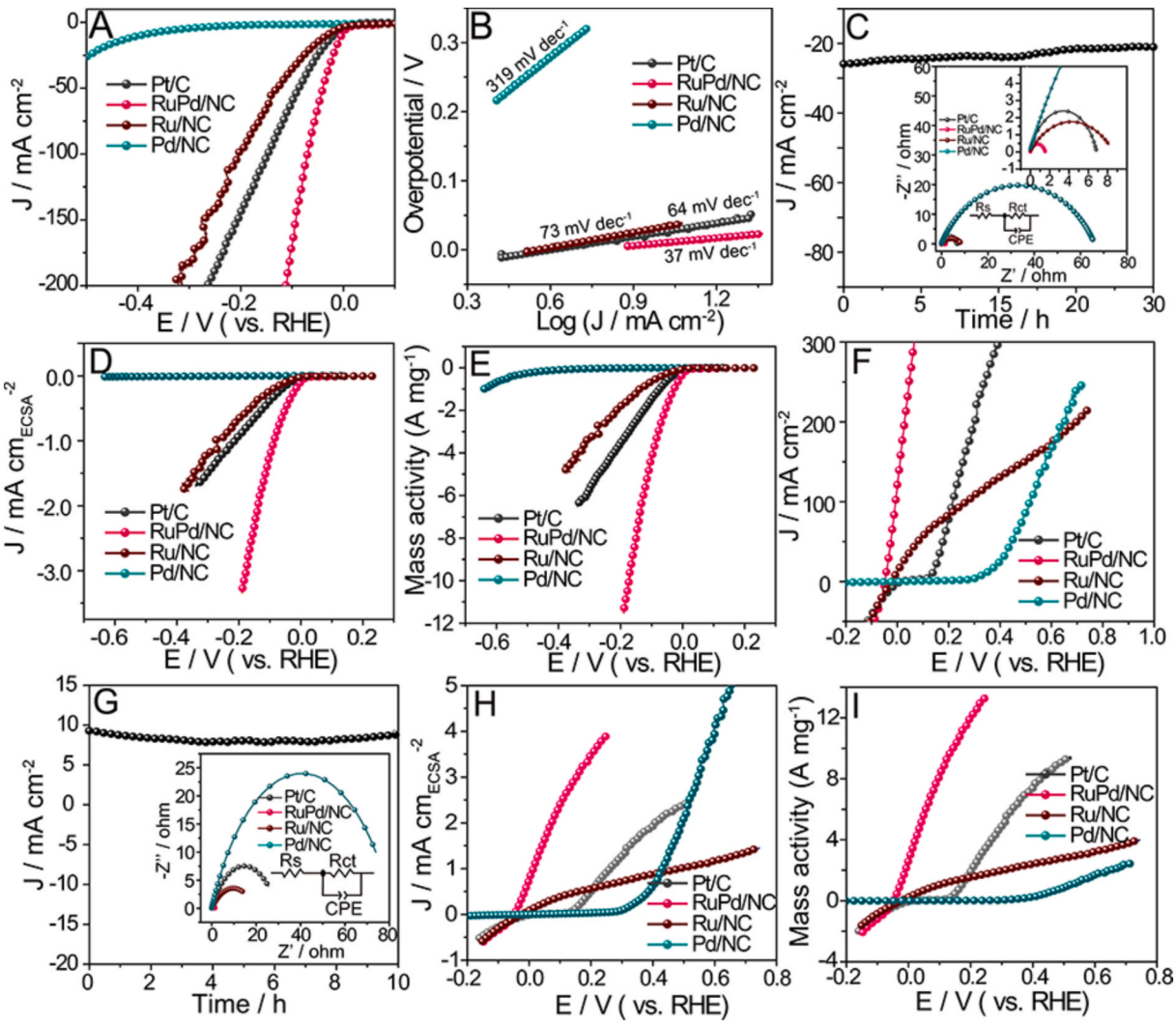

Fig. 3. (A) LSV curves, (B) Tafel slopes, (C) EIS spectra and the chronoamperometric test using RuPd/NC for alkaline HER. (D) The ECSA-normalized LSV curves and (E) the mass activity for alkaline HER. (F) LSV curves, (G) EIS spectra and the chronoamperometric test using RuPd/NC for alkaline HzOR. (H) The ECSA-normalized LSV curves and (E) the mass activity for alkaline HzOR.

3.0 (Figs. 2E and 2F), far below that of bulk Pd (CN=12), and the peak at 2.02 Å reveals Pd-N/O bond with the CN of 2.7 [35]. The XPS was also determined to inspect the elemental status on sample surface (Fig. 2G−2I, S3−S5). The survey scan of XPS (Fig. S3A) confirms the presence of C, O, N, Ru and Pd in RuPd/NC. The high-resolution spectra of Ru 3p in RuPd/NC and Ru/NC both have four peaks (Fig. 2G). In RuPd/NC, the peaks at 461.5 and 483.7 eV correlate to Ru $3p_{3/2}$ and Ru $3p_{1/2}$ of Ru^0, while the ones at 464.9 and 486.1 eV match with Ru $3p_{3/2}$ and $3p_{1/2}$ of Ru^{n+} [18]. Additionally, Fig. 2H compares the Pd 3d spectra of RuPd/NC and Pd/NC. The signals at 335.4 and 340.7 eV belong to $3d_{5/2}$ and $3d_{3/2}$ of Pd^0, and the ones at 336.6 and 342.3 eV match with Pd $3d_{5/2}$ and Pd $3d_{3/2}$ peaks of Pd^{n+} in RuPd/NC [36]. Noteworthily, the binding energy of Ru 3p in RuPd/NC shifts of 0.3 eV to lower energy region relative to Ru/NC, while the peaks of Pd 3d in RuPd/NC shift about 0.2 eV to the higher energy region compared with that of Pd/NC, arising from the RuPd alloying [37,38]. Fig. 2I exhibits N 1 s spectra of RuPd/NC with the signals at 398.8, 399.7, 400.7 and 401.6 eV correspond to the pyridinic N, metal-N bond, pyrrolic and graphitic N [39], respectively. Furthermore, the inductively coupled plasma optical emission spectrometer (ICP-OES) demonstrates 14.7 wt% Ru and 7.76 wt% Pd in RuPd/NC, compared with 26.5 wt% Ru in Ru/NC and 49.1 wt % Pd in Pd/NC.

The HER activity was firstly studied in 1 M KOH. The linear sweep voltammetry (LSV) reveals RuPd/NC only requires an ultrasmall potential of −8 mV to achieve 10 mA cm^{-2} (Fig. 3A), overmatching the benchmark Pt/C (−18 mV), Ru/NC (−33 mV) and Pd/NC (−40 mV). Moreover, RuPd/NC just requires a small overpotential of 65 mV to deliver 100mA cm^{-2}, compared with that of Pt/C (146.7 mV), demonstrating the superior HER activity at large current density. Meanwhile, RuPd/NC also has the lowest Tafel slope of 37 mV dec^{-1} (Fig. 3B), indicating the most favorable HER kinetics. The electrochemical impedance spectra (EIS) test (inset in Fig. 3C) shows a ultrasmall charge transfer resistance (R_{ct}, 1.46 Ω) for RuPd/NC, indicating the fast charge transfer and reaction dynamics. Furthermore, after 30 h's chronopotentiometric test (Fig. 3C), the current density has insignificant change on RuPd/NC, indicating its excellent stability. The electrochemical surface area (ECSA) can be evaluated from the electrical double-layer capacitance (C_{dl}), and RuPd/NC has the largest C_{dl} value (Fig. S6), suggesting the highly exposed active sites on RuPd/NC [40]. Moreover, to evaluate the intrinsic activity of different samples, the ECSA-normalized and mass-activity LSVs was extracted as shown in Figs. 3D and 3E. Concretely, RuPd/NC can attain −1.66 mA cm^{-2}_{ECSA} at −0.1 V, 4.3 and 6.9 times that of Pt/C (−0.383 mA cm^{-2}_{ECSA}) and Ru/C (−0.239 mA cm^{-2}_{ECSA}), and the mass activity of −5.74 A mg^{-1} is observed for RuPd/NC at −0.1 V, 3.9 and 8.7 times that of Pt/C (−1.47 A mg^{-1}) and Ru/C (−0.66 A mg^{-1}), respectively, those verifying the best intrinsic

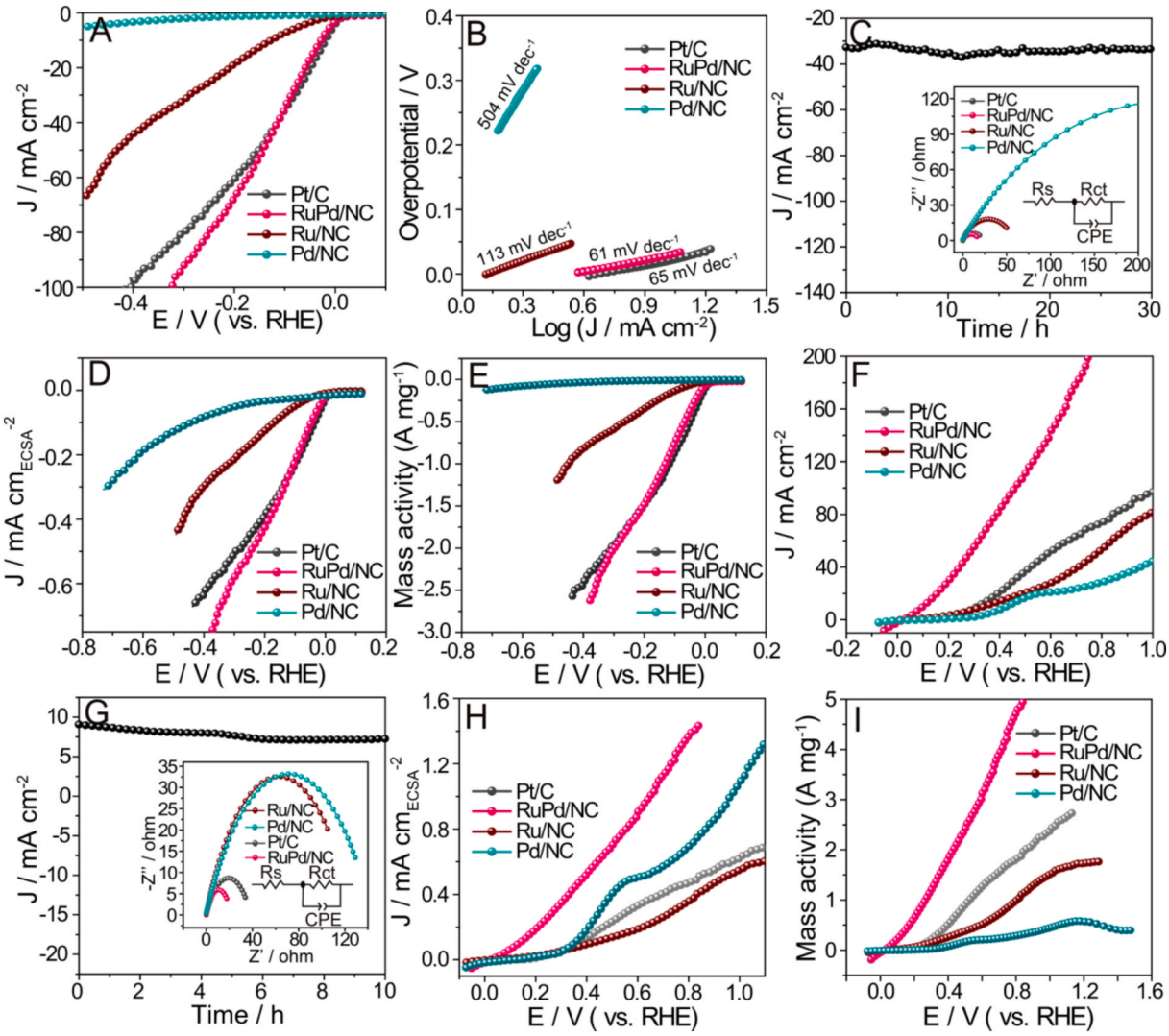

Fig. 4. (A) LSV curves, (B) Tafel slopes, (C) EIS spectra and the chronoamperometric test using RuPd/NC for neutral HER. (E) The ECSA-normalized LSV curves and (E) the mass activity for neutral HER. (F) LSV curves, (G) EIS spectra and the chronoamperometric test using RuPd/NC for neutral HzOR. (H) The ECSA-normalized LSV curves and (E) the mass activity for neutral HzOR.

activity of RuPd/NC for alkaline HER.

The HzOR activity was measured in 1.0 M KOH with 0.5 M N_2H_4 [20,41]. As depicted in Fig. 3F, LSV curves manifest the best HzOR activity on RuPd/C with a potential of −42 mV to deliver 10 mA cm^{-2}, also on a par with the most advanced materials (Table S4). Meanwhile, RuPd/C just requires an ultralow potential of 28 mV to drive 200 mA cm^{-2}, greatly surpassing Pt/C (268 mV). Besides, RuPd/NC displays the smallest Tafel slope (32 mV dec^{-1}, Fig. S7A), and the lowest R_{ct} value of 1.5 Ω (inset in Fig. 3G), verifying the most favorable HzOR kinetics. Furthermore, the current attenuation of RuPd/NC is negligible in the chronopotentiometric test for 10 h, exhibiting its excellent stability. Similarly, RuPd/NC also owns the best intrinsic activity for HzOR, with 3.47 mA cm^{-2}_{ECSA} and 11.9 A mg^{-1} for ECSA-normalized and mass activity at 0.2 V, about 7.0 and 6.3 times that of Pt/C (Figs. 3H and 3I), respectively.

The neutral HER activity of RuPd/NC in 1.0 M phosphate buffered saline (PBS, pH=7) was further studied [42,43]. As shown in Fig. 4A, the overpotential of RuPd/NC is measured to be 28 mV at 10 mA cm^{-2}, slightly inferior to Pt/C (18 mV) but far superior to Ru/NC (127 mV) and Pd/NC (662 mV). Additionally, RuPd/NC requires an overpotential of 325 mV to attain 100 mA cm^{-2}, about 86 mV less than that of Pt/C (411 mV). Fig. 4B exhibits that RuPd/NC has the smallest Tafel slope of 61 mV dec^{-1}, suggesting the fastest catalytic kinetics. RuPd/NC also owns the smallest R_{ct} value (24.1 Ω), indicating that the smoothest interfacial charge transfer during HER. Furthermore, the unchangeable chronoamperometric signal on RuPd/NC for 30 h (Fig. 4C) further verifies the remarkable stability for neutral HER. Notably, RuPd/NC also has the good intrinsic activity for neutral HER, with −0.43 mA cm^{-2}_{ECSA} and −2.00 A mg^{-1} for ECSA-normalized and mass activity at −0.2 V (Figs. 4D and 4E), comparable with those of Pt/C (−0.39 mA cm^{-2}_{ECSA} and −1.96 A mg^{-1}).

The neutral HzOR was then determined in 1.0 M PBS + 0.1 M N_2H_4 [20]. Specifically, RuPd/NC exhibits a small working potential of 100 mV to achieve 10 mA cm^{-2} (Fig. 4F), far overmatching Pt/C (312 mV). Meanwhile, the Tafel slope of RuPd/NC electrode (Fig. S7B is mere 102 mV dec^{-1}, superior to Pt/C (150 mV dec^{-1}), indicating the much better HzOR kinetics. The R_{ct} of RuPd/NC (21.6 Ω) is smaller than that of Pt/C (42.1 Ω), confirming that the RuPd/NC has a fast electron transfer and HzOR kinetics (inset of Fig. 4G). The chronoamperometric test was performed without obvious attenuation after 10 h's operation (Fig. 4G). Likewise, RuPd/NC has the best ECSA-normalized and mass activity with 0.53 mA cm^{-2}_{ECSA} and 1.82 A mg^{-1} at 0.4 V (Figs. 4H and 4I), 4.1 and 3.6 times those of Pt/C (0.13 mA cm^{-2}_{ECSA} and 0.51 A mg^{-1}), implying the superior intrinsic activity for neutral HzOR.

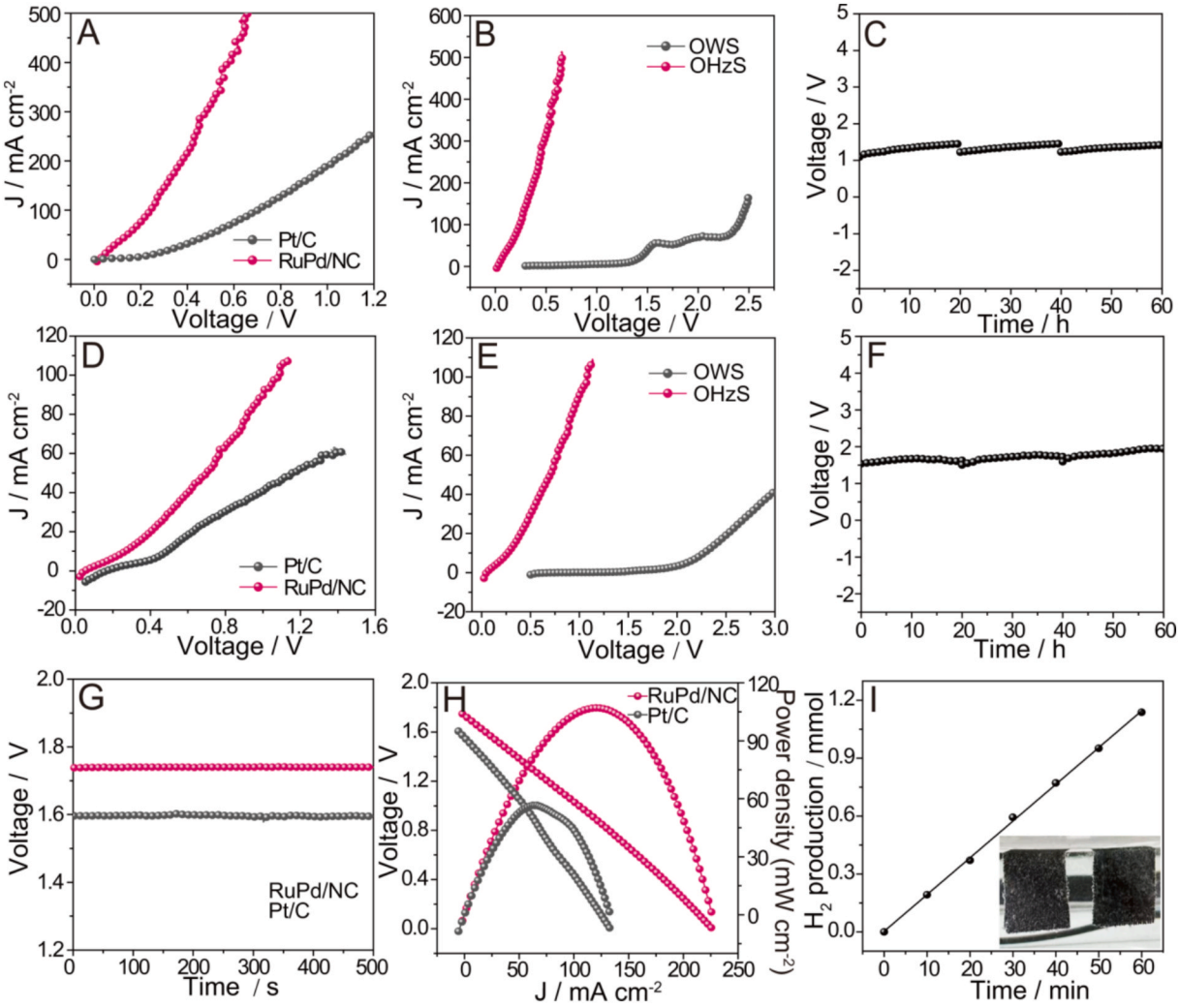

Fig. 5. LSV curves of RuPd/NC and Pt/C for (A) alkaline and (D) neutral OHzS. LSV curves of OHzS and OWS using bifunctional RuPd/NC in (B) alkaline and (E) neutral conditions. The chronopotentiometric test of OHzS for (C) alkaline and (D) neutral OHzS, with replacing electrolytes every 20 h. (G) Open circuit voltage of Pt/C||Pt/C and RuPd/NC||Pt/C DHHPFCs, (H) the power density of DHHPFCs and (I) the H_2 production with DHHPFC-powered OHzS system.

Afterwards, the two-electrode OHzS cell was assembled by using the RuPd/NC or Pt/C as bifunctional electrodes in 1.0 M KOH with 0.5 M N_2H_4 [44]. Fig. 5A presents RuPd/NC-based OHzS system separately needs ultralow voltages of 0.042 and 0.239 V to deliver 10 and 100 mA cm^{-2}, enormously better than that of Pt/C-based counterpart (0.280 and 0.716 V), and also exhibits great energy-saving advantage compared with RuPd/NC-based OWS cell (1.30 and 2.41 V, Fig. 5B). Meanwhile, the chronoamperometric curve shows the insignificant change of current density on RuPd/NC for up to for 60 h with replacing electrolyte every 20 h (Fig. 5C), verifying the robust stability of bifunctional RuPd/NC in OHzS. Furthermore, the neutral OHzS was also measured in 1.0 M PBS with 0.1 M N_2H_4. Fig. 5D displays a small voltage of 0.268 V on RuPd/NC to attain 10 mA cm^{-2}, overmatching Pt/C (0.482 V) and has an advantage of approximately 2.2 V over OWS (Fig. 5E). The neutral OHzS also has excellent stability within 60 h's continuous operation (Fig. 5F), proving the huge potential in practical applications.

The outstanding performance of RuPd/NC-based OHzS unit inspires us to further explore the practicability of economical H_2 production. As illustrated in Fig. S8a self-driven H_2 production system was built by coupling a DHHPFC with RuPd/NC as anode and commercial Pt/C as cathode to drive OHzS [45,46]. The DHHPFC shows an OCV of 1.74 V (Fig. 5G) for RuPd/NC||Pt/C-based DHHPFC with a maximum power density of 107 mW cm^{-2} (Fig. 5H), larger than those of Pt/C||Pt/C-based one (1.59 V and 56.5 mW cm^{-2}). A large number of vigorous bubbles gushed out in DHHPFC-powered OHzS with the hydrogen output of 1.13 mmol h^{-1} (Fig. 5I), proving the strong practical practicability of RuPd/NC.

To further elucidate the intrinsic origins of enhanced activity, DFT computation was performed for both HER and HzOR. Based on the aforesaid composition information, three simulated models including RuPd/NC, Ru/NC and Pd/NC were established. As known, the HER pathways can be revealed from the Tafel slopes. Figs. 3B and 4B reveal the alkaline and neutral Tafel slopes range from ~ 37 to ~ 61 mV dec^{-1}, manifesting the Volmer-Heyrovsky route for HER and the Heyrovsky reaction as the rate-determining step (RDS) [47]. Accordingly, the HER process in alkaline and neutral conditions involves water adsorption, water dissociation and H* ad-/desorption. Thus, the water dissociation energy barrier in Volmer step was firstly investigated (Fig. S9). As shown in Fig. 6A, the water dissociation energy barrier (E_w) values for Ru/NC and Pd/NC are 0.84 and 1.27 eV, respectively, and after alloying, the Ru site on RuPd/NC has the much lower E_w of 0.33 eV, superior to Pd site on RuPd/NC (0.95 eV), suggesting the water dissociation occurs on the Ru site of RuPd/NC with the most favorable kinetics [48]. Subsequently, the hydrogen adsorption free energy (ΔG_{H^*}) was also analyzed for different models [49]. As shown in Fig. 6B, on RuPd/NC, the Pd site has the better ΔG_{H^*} (−0.46 eV) relative to Ru site (−0.76 eV), manifesting the H intermediate produced by water dissociation on the Ru site of RuPd/NC will transfer to the adjacent/neighboring Pd site for desorption to

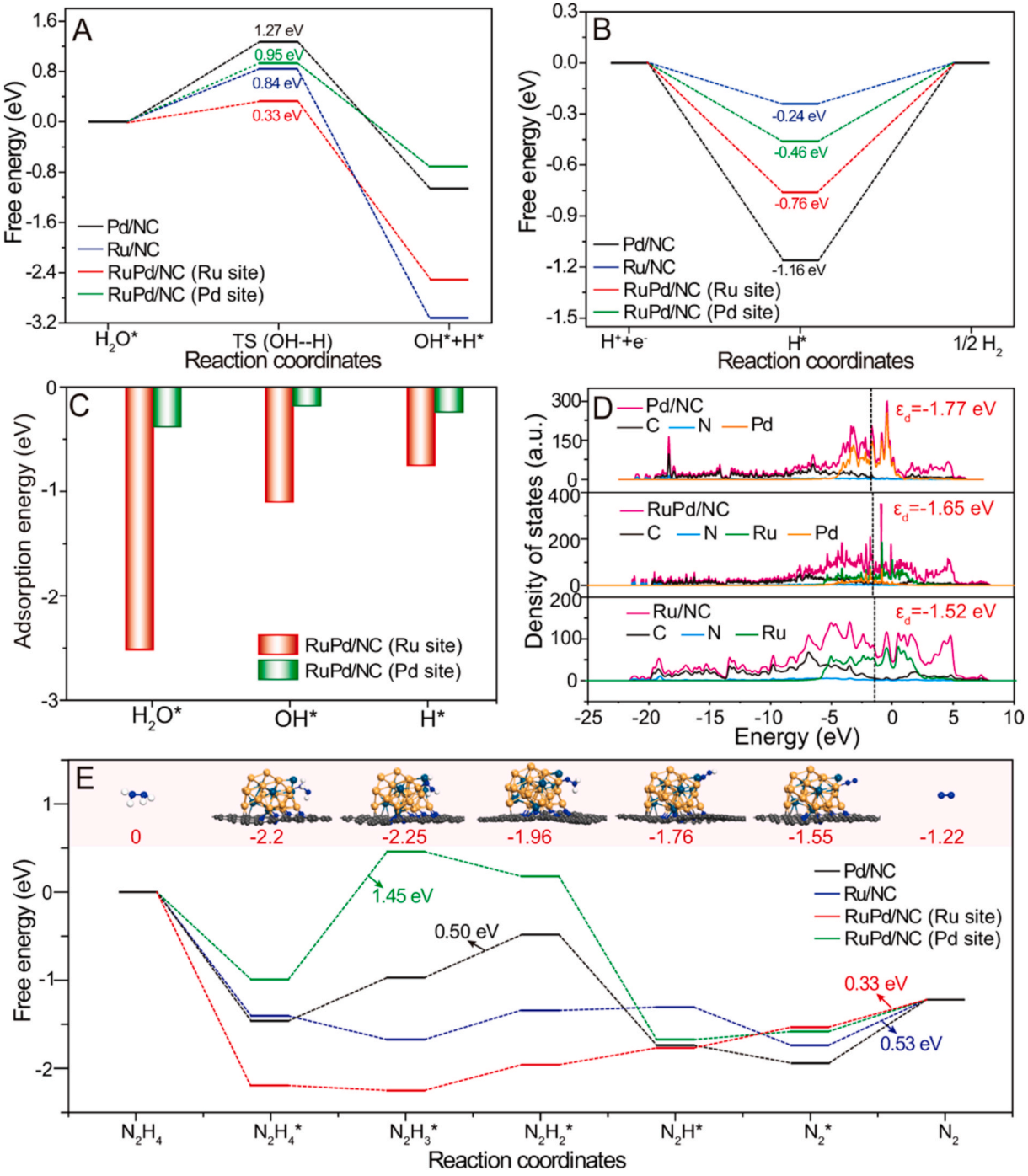

Fig. 6. (A) The calculated energy barriers of water dissociation and (B) the adsorption free energies of H* on Pd/NC, Ru/NC, RuPd/NC (Ru site) and RuPd/NC (Pd site). (C) The adsorption energy of H_2O*, OH* and H* intermediates on different models. (D) Density of states of Pd/NC, Ru/NC and RuPd/NC, black dotted line denotes the d-band center (ε_d). (E) The free energy profiles of stepwise hydrazine intermediates on Pd/NC, Ru/NC, RuPd/NC (Ru site) and RuPd/NC (Pd site). The yellow, green, gray, blue and white sphere stands for Ru, Pd, C, N and H atom, respectively. (For interpretation of the references to colour in this figure legend, the reader is referred to the web version of this article.)

generate H_2 [48]. Additionally, the adsorption energy values of H_2O*, OH* and H* intermediates on two sites of RuPd/NC were also analyzed. As shown in Fig. 6C, the Ru site of RuPd/NC has the more negative values for H_2O* and OH* adsorption energy, indicating the strong ability for water dissociation, while Pd site with the benign adsorption energy of H* can facilitate the H desorption [50]. Moreover, the moderate d-band center (ε_d) can be found on RuPd/NC (−1.65 eV, Fig. 6D) in comparison to that of Pd/NC (−1.77 eV) and Ru/NC (−1.52 eV), arising from the synergetic regulation by the alloying effect and metal-substrate interaction and enabling the more favorable balance for the ad-/desorption in electrocatalytic process [41].

The theoretical mechanism of HzOR was also interpreted by DFT calculations [51]. The free energy of HzOR intermediates in stepwise dehydrogenation processes was examined carefully on different models (Fig. 6E and S10). Notably, the N_2H_4 adsorption is downhill and spontaneous, while the desorption of N_2 is uphill and non-spontaneous on all models. More specifically, the dehydrogenation of N_2H_3* to N_2H_2* is the RDS for Pd/NC with the activation energy of 0.50 eV, while the RDS on

RuPd/C (Pd site) is the step of N_2H_4* to N_2H_3* with the uphill energy of 1.45 eV, and Ru/NC and RuPd/NC (Ru site) share the same RDS as the final desorption of N_2 with the activation energy of 0.53 and 0.33 eV, respectively [52,53]. Evidently, RuPd/NC has the highest HzOR activity with Ru as active sites. These results demonstrate alloying of Ru and Pd can validly tailor electronic property of active sites, accordingly optimizing the thermodynamic parameters for water dissociation and H desorption in HER and intermediate steps in HzOR.

4. Conclusions

In conclusion, a new-type RuPd/NC was facilely synthesized by simple mixing and pyrolysis only with $Ru(bpy)_3Cl_2$ and $Pd(bpy)Cl_2$ as precursors. Remarkably, RuPd/NC displays superior bifunctional performance for HER and HzOR in nonacidic conditions with better ECSA-normalized and mass activity in comparison to Pt/C. Moreover, the two-electrode OHzS systems in both electrolytes show great energy-efficient advantages over OWS, and a home-made DHHPFC can easily power the OHzS cell for the self-driven H_2 production system. DFT computations uncover the root of improved bifunctional activity lies in the synergistic regulation of alloying effect and metal-substrate interaction, endowing RuPd/NC with the greatly lowered water dissociation energy barrier at Ru site followed by the H desorption on the adjacent Pd site for HER and the reduced activation energy on Ru site for HzOR.

CRediT authorship contribution statement

Qijing Zhang: Writing – original draft, Investigation, Conceptualization. **Hongxia Yu:** Validation, Methodology. **Siyi Wang:** Investigation, Formal analysis. **Haibo Li:** Validation, Funding acquisition. **Suyuan Zeng:** Visualization, Formal analysis. **Rui Li:** Software. **Qingxia Yao:** Methodology, Data curation. **Qi Zhang:** Funding acquisition, Conceptualization. **Ruru Chen:** Writing – review & editing, Project administration. **Lijian Meng:** Writing – review & editing, Resources. **Konggang Qu:** Writing – review & editing, Supervision, Funding acquisition.

Declaration of competing interest

The authors declare that they have no known competing financial interests or personal relationships that could have appeared to influence the work reported in this paper.

Acknowledgements

This work was financially supported by the National Natural Science Foundation of China (52303185), Natural Science Foundation of Shandong Province (ZR2025MS233, ZR2022MB137 and ZR2021MB122) and Doctoral Program of Liaocheng University (318051608).

Appendix A. Supplementary data

Supplementary data to this article can be found online at https://doi.org/10.1016/j.fuel.2025.137768.

Data availability

Data will be made available on request.

References

[1] Turner JA. Sustainable Hydrogen Production. Science 2004;305(5686):972–4.
[2] Sher Shah MSA, Jang GY, Zhang K, Park JH. Transition metal carbide-based nanostructures for electrochemical hydrogen and oxygen evolution reactions. EcoEnergy 2023;1(2):344–74.
[3] Fu X, Li H, Zong Y, Xiao W, Wang J, Li H, et al. Ultrafast Construct Local Acidic Microenvironment of Boron-Intercalated Osmium with Anti-Precipitation and Corrosion-Resistant for Seawater-splitting. Angew Chem Int Ed 2025;64(40):e202512710.
[4] Fu X, Zang X, Gao J, Li H, Xiao W, Zong Y, et al. Ultrafast Microwave Quasi-Solid-State Construction of Os-OsP_2 with Enhanced Interfacial Spillover for Seawater-Based Anion Exchange Membrane Electrolyzers. Adv Energy Mater 2025;15(30):2501054.
[5] Yang S, Wu C, Wang J, Shen H, Zhu K, Zhang X, et al. Metal Single-Atom and Nanoparticle Double-Active-Site Relay Catalysts: Design, Preparation, and Application to the Oxidation of 5-Hydroxymethylfurfural. ACS Catal 2022;12(2):971–81.
[6] Zhang J-Y, He T, Wang M, Qi R, Yan Y, Dong Z, et al. Energy-saving hydrogen production coupling urea oxidation over a bifunctional nickel-molybdenum nanotube array. Nano Energy 2019;60:894–902.
[7] Fan C, Zhang M, Sun Y, Wang L, Wang Y-Q. Rapid B-Ni charge transfer pathway induced Ni3+/Ni2+ sites reversible conversions enabling efficient urea oxidation assisted hydrogen production. J Colloid Interf Sci 2025;690:137355.
[8] Liu G, Zhao C, Wang G, Zhang Y, Zhang H. Efficiently electrocatalytic oxidation of benzyl alcohol for energy- saved zinc-air battery using a multifunctional nickel–cobalt alloy electrocatalyst. J Colloid Interf Sci 2018;532:37–46.
[9] Yu H, Wang W, Mao Q, Deng K, Wang Z, Xu Y, et al. Pt single atom captured by oxygen vacancy-rich NiCo layered double hydroxides for coupling hydrogen evolution with selective oxidation of glycerol to formate. Appl Catal B Environ 2023;330:122617.
[10] Jiang N, You B, Boonstra R, Terrero Rodriguez IM, Sun Y. Integrating Electrocatalytic 5-Hydroxymethylfurfural Oxidation and Hydrogen Production via Co–P-Derived Electrocatalysts. ACS Energy Lett 2016;1(2):386–90.
[11] You B, Liu X, Jiang N, Sun Y. A General Strategy for Decoupled Hydrogen Production from Water Splitting by Integrating Oxidative Biomass Valorization. J Am Chem Soc 2016;138(41):13639–46.
[12] Zhao Y, Sun Y, Li H, Zeng S, Li R, Yao Q, et al. Highly enhanced hydrazine oxidation on bifunctional Ni tailored by alloying for energy-efficient hydrogen production. J Colloid Interf Sci 2023;652:1848–56.
[13] Burshtein TY, Yasman Y, Muñoz-Moene L, Zagal JH, Eisenberg D. Hydrazine Oxidation Electrocatalysis. ACS Catal 2024;14(4):2264–83.
[14] Zhu Y, Zhang J, Qian Q, Li Y, Li Z, Liu Y, et al. Dual Nanoislands on Ni/C Hybrid Nanosheet Activate Superior Hydrazine Oxidation-Assisted High-Efficiency H2 production. Angew Chem Int Ed 2022;61(2):e202113082.
[15] Xu J, Zhong M, Qi R, Xu M, Wang C, Lu X. Nanofibrous Ru/SnO2 heterostructure as robust bifunctional electrocatalyst for high-performance overall hydrazine splitting and Zn-hydrazine battery. J Colloid Interf Sci 2025;684:43–51.
[16] Li Y, Zhang J, Liu Y, Qian Q, Li Z, Zhu Y, et al. Partially exposed RuP2 surface in hybrid structure endows its bifunctionality for hydrazine oxidation and hydrogen evolution catalysis. Sci Adv 2020;6(44):eabb4197.
[17] Guo F, Macdonald TJ, Sobrido AJ, Liu L, Feng J, He G. Recent advances in Ultralow-Pt-Loading Electrocatalysts for the Efficient Hydrogen Evolution. Adv Sci 2023;10(21):2301098.
[18] Qu K-G, Chen Z-F, Wang L-H, Li H-B, Zeng S-Y, Li R, et al. Covalent organic framework assisted low-content ultrafine Ru on porous N-doped carbon for efficient hydrogen evolution reaction. Rare Met 2025;44(3):2094–102.
[19] Wu Z, Li Q, Xu G, Jin W, Xiao W, Li Z, et al. Microwave Phosphine-Plasma-Assisted Ultrafast Synthesis of Halogen-Doped Ru/RuP2 with Surface Intermediate Adsorption Modulation for Efficient Alkaline Hydrogen Evolution Reaction. Adv Mater 2024;36(13):2311018.
[20] Guan X, Sun Y, Zhao S, Li H, Zeng S, Yao Q, et al. Selectively nucleotide-derived RuP on N,P-codoped carbon with engineered mesopores for energy-efficient hydrogen production assisted by hydrazine oxidation. SusMat 2024;4(1):166–77.
[21] Wang Y, Li J, Yang P, Li H, Xu G, Du Y, et al. Interfacial Ru nanoclusters in tandem with single atoms on oxygen-vacancy regulated CeO2 for anion exchange membrane seawater-splitting. J Energy Chem 2025;102:618–27.
[22] Cui Z, Jiao W, Huang Z, Chen G, Zhang B, Han Y, et al. Design and Synthesis of Noble Metal-based Alloy Electrocatalysts and their Application in Hydrogen Evolution Reaction. Small 2023;19(35):2301465.
[23] Zhou Y-N, Yu W-L, Liu H-J, Fan R-Y, Han G-Q, Dong B, et al. Self-integration exactly constructing oxygen-modified MoNi alloys for efficient hydrogen evolution. EcoEnergy 2023;1(2):425–36.
[24] Sheng Y, Xie J, Yang R, Yu H, Deng K, Wang J, et al. Modulating Hydrogen Adsorption by Unconventional p–d Orbital Hybridization over Porous High-Entropy Alloy Metallene for Efficient Electrosynthesis of Nylon-6 Precursor. Angew Chem Int Ed 2024;63(44):e202410442.
[25] Gerber IC, Serp P. A Theory/Experience Description of support Effects in Carbon-Supported Catalysts. Chem Rev 2020;120(2):1250–349.
[26] Wang J, Guan X, Li H, Zeng S, Li R, Yao Q, et al. Robust Ru-N metal-support interaction to promote self-powered H2 production assisted by hydrazine oxidation. Nano Energy 2022;100:107467.
[27] Guan X, Wu Q, Li H, Zeng S, Yao Q, Li R, et al. Identifying the roles of Ru single atoms and nanoclusters for energy-efficient hydrogen production assisted by electrocatalytic hydrazine oxidation. Appl Catal B Environ 2023;323:122145.
[28] Ling H, Yuan Q, Sheng T, Wang X. Dual active site and metal–substrate interface effect endow platinum–ruthenium/molybdenum carbide efficient pH-universal hydrogen evolution reaction. J Colloid Interface Sci 2025;685:371–81.
[29] Mironenko RM, Belskaya OB, Gulyaeva TI, Trenikhin MV, Nizovskii AI, Kalinkin AV, et al. Liquid-phase hydrogenation of benzaldehyde over Pd-Ru/C catalysts: Synergistic effect between supported metals. Catal Today 2017;279:2–9.
[30] Mitra A, Jana D, De G. Synthesis of Equimolar Pd–Ru Alloy Nanoparticles Incorporated Mesoporous Alumina Films: a High Performance Reusable Film Catalyst. Ind Eng Chem Res 2013;52(45):15817–23.

[31] Shen R, Liu Y, Zhang H, Liu S, Wei H, Yuan H, et al. Coupling oxygen vacancy and hetero-phase junction for boosting catalytic activity of Pd toward hydrogen generation. Appl Catal B Environ 2023;328:122484.
[32] Zhao M, Lyu Z, Xie M, Hood ZD, Cao Z, Chi M, et al. Pd-Ru Alloy Nanocages with a Face-Centered Cubic Structure and their Enhanced activity toward the Oxidation of Ethylene Glycol and Glycerol. Small Methods 2020;4(5):1900843.
[33] Yu Q, Wang J, Li H, Li R, Zeng S, Li R, et al. Natural DNA-derived highly-graphitic N, P, S-tridoped carbon nanosheets for multiple electrocatalytic applications. Chem Eng J 2022;429:132102.
[34] Qi H, Yang J, Liu F, Zhang L, Yang J, Liu X, et al. Highly selective and robust single-atom catalyst Ru1/NC for reductive amination of aldehydes/ketones. Nat Commun 2021;12(1):3295.
[35] Li W, Chu X-s, Wang F, Dang Y-y, Liu X-y, Ma T-h, et al. Pd single-atom decorated CdS nanocatalyst for highly efficient overall water splitting under simulated solar light. Appl Catal B Environ 2022;304:121000.
[36] Guo Z, Wang R, Guo Y, Jiang J, Wang Z, Li W, et al. Controlled Synthesis of Palladium Phosphides with Tunable Crystal Phases and their Sulfur-Tolerant Performance. ACS Catal 2022;12(24):15193–206.
[37] Tang M, Mao S, Li M, Wei Z, Xu F, Li H, et al. RuPd Alloy Nanoparticles Supported on N-Doped Carbon as an Efficient and Stable Catalyst for Benzoic Acid Hydrogenation. ACS Catal 2015;5(5):3100–7.
[38] Zhao S, Zhang Y, Li H, Zeng S, Li R, Yao Q, et al. Regulating Ru active Sites by Pd alloying to significantly Enhance Hydrazine Oxidation for Energy-saving Hydrogen Production. J Mater Chem A 2023;11:13783–92.
[39] Liu G, Chen Y, Chen Y, Shi Y, Zhang M, Shen G, et al. Indirect Electrocatalysis S—N/S—S Bond Construction by Robust Polyoxometalate based Foams. Adv Mater 2023;35(40):2304716.
[40] Li J, Zhang C, Zhang C, Ma H, Guo Z, Zhong C, et al. Green Electrosynthesis of 5,5′-Azotetrazolate energetic Materials Plus Energy-Efficient Hydrogen Production using Ruthenium Single-Atom Catalysts. Adv Mater 2022;34(32):2203900.
[41] Qian Q, Zhang J, Li J, Li Y, Jin X, Zhu Y, et al. Artificial Heterointerfaces Achieve Delicate Reaction Kinetics towards Hydrogen Evolution and Hydrazine Oxidation Catalysis. Angew Chem Int Ed 2021;60(11):5984–93.
[42] Zhou J, Xie Y, Yang L, Liu Y, Du Y, Yu L, et al. Development and perspectives of multi-site electrocatalysts for neutral hydrogen evolution. Inorg Chem Front 2023;10(10):2842–59.
[43] Sun K, Wu X, Zhuang Z, Liu L, Fang J, Zeng L, et al. Interfacial water engineering boosts neutral water reduction. Nat Commun 2022;13(1):6260.
[44] Sun F, Qin J, Wang Z, Yu M, Wu X, Sun X, et al. Energy-saving hydrogen production by chlorine-free hybrid seawater splitting coupling hydrazine degradation. Nat Commun 2021;12(1):4182.
[45] Khalafallah D, Zhi M, Hong Z. Development Trends on Nickel-based Electrocatalysts for Direct Hydrazine fuel Cells. ChemCatChem 2021;13(1):81–110.
[46] Zabielaitė A, Balčiūnaitė A, Šimkūnaitė D, Lichušina S, Stalnionienė I, Šimkūnaitė-Stanynienė B, et al. High Performance Direct N2H4-H2O2 fuel Cell using Fiber-shaped Co decorated with Pt Crystallites as Anode Electrocatalysts. J Electrochem Soc 2020;167(5):054502.
[47] Deng R, Guo M, Wang C, Zhang Q. Recent advances in cobalt phosphide-based materials for electrocatalytic water splitting: from catalytic mechanism and synthesis method to optimization design. Nano Mater Sci 2024;6(2):139–73.
[48] Cheng C, Chen F, Zhang B, Zhao B-H, Du X. Promoting Water Dissociation and weakening active Hydrogen Adsorption to boost the Hydrogen transfer Reaction over a Cu−Ag Superlattice Electrocatalyst. Angew Chem Int Ed 2025;64(1):e202413897.
[49] Liu Q, Fu X, Li H, Xing J, Xiao W, Zong Y, et al. Microwave quasi-solid-constructed Ni2P–Ni12P5-supported Os with unique metal–support interaction for anion-exchange membrane seawater electrolysis. Chem Sci 2025;16(29):13306–15.
[50] Lin Q, Liu Y, Li J, Feng K, Zhong J, Huang H, et al. Enhanced acidic hydrogen evolution reaction kinetics via nitrogen-doped iridium nanosheet with optimized hydrogen adsorption energy. Chem Eng J 2024;495:153214.
[51] Li J, Li Y, Wang J, Zhang C, Ma H, Zhu C, et al. Elucidating the critical Role of Ruthenium Single Atom Sites in Water Dissociation and Dehydrogenation Behaviors for Robust Hydrazine Oxidation-Boosted Alkaline Hydrogen Evolution. Adv Funct Mater 2022;32(16):2109439.
[52] Liu G, Nie T, Wang H, Shen T, Sun X, Bai S, et al. Size Sensitivity of Supported Palladium Species on Layered double Hydroxides for the Electro-oxidation Dehydrogenation of Hydrazine: from Nanoparticles to Nanoclusters and Single Atoms. ACS Catal 2022;12(17):10711–7.
[53] Hu Y, Chao T, Li Y, Liu P, Zhao T, Yu G, et al. Cooperative Ni(Co)-Ru-P Sites Activate Dehydrogenation for Hydrazine Oxidation Assisting Self-powered H2 production. Angew Chem Int Ed 2023;62(35):e202308800.